Characterising the composition of olivine and iron oxides in a sample of the Sericho meteorite by Raman spectroscopy using Principal Component Analysis

Cedric MALHERBE[1,2], Ian B. HUTCHINSON[2], Hannah N. LERMAN[2], Melissa MCHUGH[2] and Gauthier EPPE[1]

(1) Mass Spectrometry Laboratory, MolSys RU, University of Liège, Liège, Belgium
(2) Department of Physics and Astronomy, University of Leicester, Leicester, United Kingdom

Corresponding author: c.malherbe@uliege.be

Abstract

Raman spectroscopy is a key technique for planetary exploration, providing mineralogical insights under strict constraints on power, mass, and data transmission. This study applies Principal Component Analysis (PCA) to Raman imaging data from the Sericho pallasite meteorite, composed mainly of Mg-rich olivine and Fe-Ni alloy. PCA efficiently reduced the complex dataset to only five principal components retaining most of the molecular information. Using PCA scores, averaged Raman spectra were calculated to significantly simplifying spectral interpretation, highlighting olivine as the dominant mineral and goethite, disordered hematite as well as disordered carbon as minor phases in the sample. In addition, PCA scores associated with the x-y coordinate of the Raman image enables identifying distinct mineralogical domains revealing the spatial distribution of iron oxyhydroxides primarily at interfaces and fractures of the olivine inclusions. Additionally, PCA-filtered spectra enabled spatially resolved quantification of olivine composition, showing a 5–10% magnesium enrichment in olivine cores compared to interfaces with iron oxyhydroxides, suggesting weathering origins of the Fe-Ni alloy. These results demonstrate the strong potential of PCA for data reduction, visualization, and interpretation of complex Raman datasets, making it a powerful tool for *in situ* mineralogical analysis during future robotic or human planetary missions where fast real-time data processing is key for informed decision-making.

Introduction

Miniaturised Raman instruments have been developed for planetary missions to Mars (e.g., SuperCam and SHERLOC on board of NASA's Mars2020 mission [1-2], and the RLS to be launch as part of the ESA's ExoMars mission[3]), to Martian moon Phobos (e.g., RAX as part of the JAXA's mission [4]) and to the Moon (NASA's Artemis and ESA's ISRU missions [5]), as they can detect geological materials within the rocky surface, including inorganic molecules and inorganic molecular ions. On Mars, Raman data can provide important information on the habitability of the planetary surface environment. In addition to identifying mineralogical compositions, Raman spectroscopy can also detect organic carbonaceous molecules, including potential biologically derived substances from extant or extinct organisms (often referred to as biomarkers in astrobiology), or thermally processed carbonaceous compounds, such as amorphous carbon and kerogens [6].

As a non-destructive and non-invasive technique, Raman spectroscopy has recently started to play a central role in planetary exploration missions [1-6], particularly in selecting samples for further in-depth molecular analysis, for instance using mass spectrometry, which is included in the ExoMars rover payload and capable of detecting trace organics but in a partially destructive process [7]. Raman spectroscopy has been successfully applied to identify mineral phases in a wide range of space-analogue materials, including carbonates, silicates (e.g., cherts, igneous rocks, mudstones), iron oxyhydroxides, and hydrated sulphates [8-11]. In preparation for planetary missions, Raman instruments are designed within strict power, mass, volume, and data budget constraints. Therefore, evaluating their detection capabilities within these engineering constraints is essential and to inform key technical trade-off studies extensive testing must be conducted on terrestrial space-analogue samples relevant to various planetary scenarios using both laboratory-based and flight-like spectrometers [8-12].

Raman molecular imaging has emerged as a powerful technique for characterising the variation of geochemical composition across heterogeneous sample sections, including microstructures such as mineral grains and inclusions or, in some cases, preserved biomarkers. Visualising local molecular composition at the interfaces between mineral phases is particularly valuable, as it can reveal historical changes in the microenvironment of a sample during its formation or subsequent weathering, both key objectives of future planetary exploration missions. While Raman spectrometers have been deployed for space missions as discussed above, Raman imagers (i.e., Raman instrument specifically operated to produce Raman images) had not been proposed for space missions, particularly due to the challenges associated with the preparation of flat and polished surface of the samples, the (micro)focussing/collection optics on the sample surfaces, and of storing and transmitting large data sets to Earth (i.e., which would not comply with the engineering budget constraints of such robotic missions). Typically, Raman images are constructed by identifying the intensity of specific Raman signatures (using for instance a colour coded scale) at different *x,y* coordinates on the sample surface, requiring the acquisition of hundreds of spectra [13], however, only a few spectra would comply with the budget requirement. Moreover, in complex heterogeneous samples, Raman signatures from multiple mineral phases are often observed simultaneously in one spectrum and frequently overlap, complicating the interpretation of the data [14].

In preparation for future human planetary exploration missions, where trained astronauts will operate dedicated Raman instruments, simple yet effective data processing methods that can reduce the complexity or amount of data could enable the integration of Raman imaging into instrument payloads. The ESA's PANGAEA training programme is exploring such approaches [15]. In this context, Principal Component Analysis (PCA) is a readily implementable, unsupervised multivariate statistical analysis that offers a robust solution for data reduction [16]. PCA transforms the original correlated spectroscopic variables (i.e., the wavenumbers at which Raman signals are recorded) into a new set of uncorrelated variables, known as the principal components (PCs). These PCs are calculated as linear combinations of the initial spectroscopic variables and are arranged so that each successive PC captures the maximum remaining variability in the dataset, respectively. Because the PCs are orthogonal to each other, the variability explained by one PC is independent of the variability explained by the other PCs, allowing for a reduction in data complexity while keeping the most informative spectroscopic information [17].

In this publication, we discuss the implementation of PCA as a tool to reduce the data set to subset of a few spectra containing the most relevant molecular information and to identify underlying molecular signatures associated with minerals present in the olivine inclusions of a sample of the Sericho meteorite. Furthermore, we used PCA loadings to generate images that reveal the spatial distribution and co-location of minerals in the sample, comparing these images with conventional Raman images based on single-band intensity mapping. Finally, by analysing averaged Raman spectra for olivine-rich regions of interest, we investigate compositional variations in the olivine inclusions, revealing changes in iron content from the edges to the centre of the inclusions.

Materials and Methods

A polished 4 cm^2 slice (5 mm thick) of the Sericho meteorite was interrogated. The 2.8 tons Sericho meteorite was discovered in Kenya near the city of Sericho and was recorded in 2017 as a pallasite, a stony-iron meteorite constituted of a metallic core of iron and nickel alloy with inclusions of olivine ranging from 0.5 to 1.5 cm in size (as shown in Figure 1A) [18,19]. Olivine is a solid solution of forsterite (Mg_2SiO_4) and fayalite (Fe_2SiO_4) and the olivine inclusions of the Sericho pallasite have been reported to contain an average of 87.7% of forsterite [20]. Besides olivine, some minor minerals were reported for the Sericho pallasite such as merrillite, stanfieldite or troilite.

Raman spectra were recorded using a Labram 300 spectrometer (Horiba), interfaced with a 532.3 nm DPSS laser (typically delivering between 0.4 and 4 mW of power to the sample for this study to avoid phase transition of goethite) and a thermoelectrically cooled CCD detector Andor iDus DU401 BRDD. Data were obtained across the 200-2000 cm^{-1} wavenumber offset range, with a spectral resolution of ~3 cm^{-1}. The laser footprint on the sample was ~4 µm in diameter (through an objective Olympus X50, NA 0.50). All Raman spectra were baseline-corrected using fourth order polynomial fitting with the LabSpec 5.78 software (Horiba) to remove the autofluorescence background without removing broad Raman features, especially those associated with distorted carbon.

Principal Component Analysis (PCA) was performed on the Raman images using PAST 4.16 freeware [21], using the correlation matrix. The PCA analysis was conducted after unwrapping the Raman spectra, meaning that the spatial proximity of pixels where spectra were recorded was not considered *a priori* in the computation. To account for variations in intensity due to differences in Raman cross-sections among mineral phases, all Raman spectra processed by PCA in the images were normalized to their maximum intensity.

Results and discussion

Microscopic observations of the Sericho pallasite slice revealed that the olivine inclusions were inhomogeneous, displaying microfractures and micrometric inclusions, as shown in Figure 1. Raman spectra were obtained for these microstructures and representative Raman spectra from the sample are shown in Figure 1D. Spectral identification was performed based on the occurrence of characteristic Raman bands and their relative intensities, relying on reference samples from mineral collections or, when appropriate reference samples were not available in the laboratory, from open databases [22]. The data confirmed the presence of Mg-rich olivine (Mg_2SiO_4, characteristic bands at 823 and 855 cm^{-1}), goethite (FeO(OH), characteristic bands at 299, 393, and 555 cm^{-1}), disordered carbon (C, characteristic at 1360 and 1600 cm^{-1}) and disordered hematite (Fe_2O_3, characteristic bands at 292, 410, 500, 610, 660 and 1320 cm^{-1}). Disordered hematite is characterized by a broadening of the Raman signature of crystallised hematite (292, 410, 500, 610 and 1320 cm^{-1}) [23], and the appearance of the band at 660 cm^{-1} due to breaking of the symmetry [24]. The band has also been attributed to the presence of either magnetite (Fe_3O_4) or maghemite (Fe_2O_3), which is an allotrope of hematite. However, magnetite would require a large amount of magnetite to be observed at 660 cm^{-1} along hematite or goethite [25], in which case Raman bands at 310 and 540 cm^{-1} would also be observed [26].

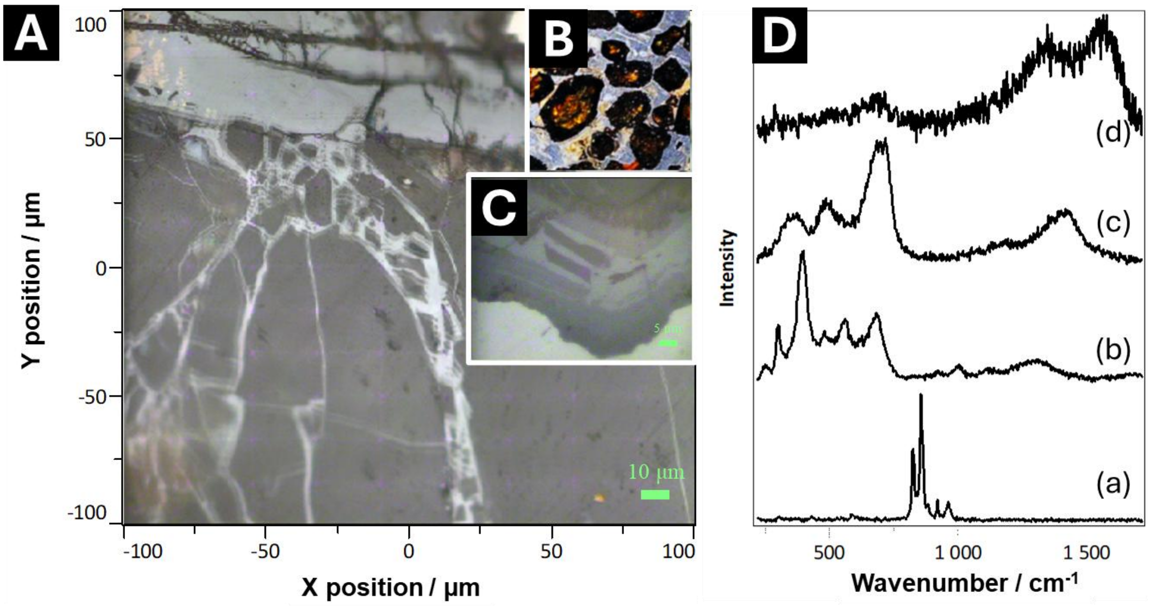

Figure 1. *(A) Micrography of the interface between an olivine inclusion (grey area) showing various microfractures (white) and the iron-nickel alloy (clear area at the top of the image). (B) Picture of the olivine inclusions on the Sericho pallasite slice (1 cm by 1 cm). (C) Micrography showing micrometric inclusions in olivine. (D) Representative baseline-corrected Raman spectra recorded for specific microstructure on the sample surface: (a) Raman spectrum of olivine, (b) Raman spectrum of goethite, (c) Raman spectrum of disordered hematite and (d) Raman spectrum of carbonaceous matter (disordered carbon).*

The presence of olivine as the main mineral constituent of the inclusions was expected for a pallasite. Goethite and disordered hematite appear to have formed at the interface with the Fe-Ni alloy, possibly filling microfractures due to oxidation, leaching and precipitation that might have happened by weathering process after the Sericho meteorite landing on the Earth surface. These iron oxides were observed exclusively near the olivine-metal interface. The identification of goethite and disordered hematite is not as straightforward as the identification of olivine as their Raman cross-sections are lower, and their Raman signals are partially absorbed before reaching the collection lens, decreasing the signal-to-noise ratio. Consequently, relative Raman intensities varied depending on the sample location, as shown in Figure 2. In addition, the Raman signatures of goethite and disordered hematite often appeared overlapped. In some spectra, only the broad 610-660 cm^{-1} and 1300 cm^{-1} bands of disordered hematite were readily observed.

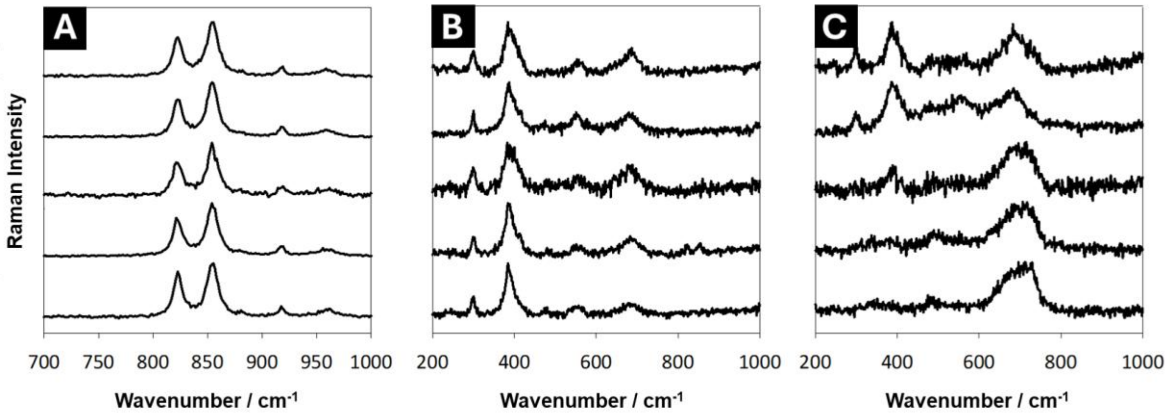

Figure 2. *Raman spectra recorded randomly and attributed to (A) olivine, (B) goethite and (C) disordered hematite, sometimes overlapped with goethite (top two spectra).*

Disordered carbon was detected in a few black areas on the sample surface, as shown in Figure 3A. Raman imaging was performed on the blue framed region of interest highlighted in Figure 3A, and Raman images were generated by tracking the intensity of signals associated with carbon (Figure 3C), goethite (Figure 3D) and olivine (Figure 3E). The specific Raman bands used to generate these images are shown in Figure 3B. The Raman signature of disordered carbon was always found in association with goethite/disordered hematite, though goethite was not necessarily associated with disordered carbon. Here again, goethite appears to fill the microfractures observed in the olivine. The origin of the disordered carbon remains uncertain. It could be exogenous, introduced as contamination during sample slicing and polishing or due to weathering before its official retrieval in 2016. Alternatively, it could be endogenous, representing organic material trapped within the pallasite during its formation and subsequently thermally processed upon atmospheric entry.

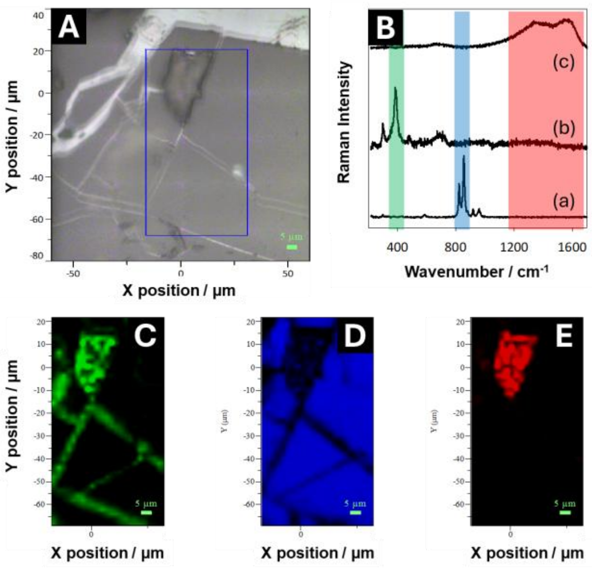

Figure 3. (A) *Micrography of a region of interest where black areas were observed. (B) Raman spectra of (a) olivine, (b) goethite and (c) disordered carbon in the region of interest shown in (A). (C)(D)(C) Raman images associated to the presence of goethite, olivine and disordered carbon respectively. These images were generated for the signals in the spectra region in green (340-440 cm^{-1}), blue (790-900 cm^{-1}) and red (1200-1700 cm^{-1}) shown in (B) respectively.*

Figure 4A shows a region of interest that appears more complex than the one shown in Figure 3A: while Figure 3A displays large monophasic domains, Figure 4A reveals multiple micrometric inclusions. These inclusions are comparable in size to the laser footprint at the surface of the sample (~ 4µm in diameter), which defines the pixel size of the Raman image; due to the size of the excitation spot, the laser likely interrogated several mineral phases at the same time, leading to overlapping signals. Moreover, as the relative intensities of the Raman signatures of each mineral can vary, artifacts were potentially introduced into the Raman images that were generated. A total of 1200 spectra were acquired from a 0.2 mm^2 region on the surface. Based on the Raman signal only (i.e. without referring to the context image), regions of interest can be defined by the operator by screening the average spectrum (Figure 4F) with a cursor and see if different area of the image is highlighted for specific wavenumbers or specific ranges of wavenumbers. Doing so, four Raman images were generated by tracing the signal intensity within specific wavenumber ranges: between 805 and 890 cm^{-1}, where the two characteristic bands of olivine are observed (Figure 4B); between 340 and 440 cm^{-1}, where the more intense characteristic band of goethite is observed (Figure 4C); between 600 and 780 cm^{-1}, where the most intense characteristic bands of disordered hematite are observed (Figure 4D); and between 450 and 600 cm^{-1}, where the characteristic bands of goethite and disordered hematite strongly overlap (Figure 4E). Olivine, whose Raman signals do not overlap with those of the other minerals in the sample, is clearly the dominant constituent of the inclusions in the Sericho pallasite (Figure 4B). The main constituent of the other part of the inclusion is goethite (Figure 4C), with some occurrence of disordered hematite, especially in contact with the olivine (Figure 4D). The last Raman image (Figure 4E) indicates that the interface layer between the Fe-Ni alloy and the olivine (~40 µm thick) is dominated by oxyhydroxides of iron. However, due to the strong spectral overlap in the 450–600 cm^{-1} range, it is not possible to distinguish between the three specific mineral phases that contribute to the Raman signal.

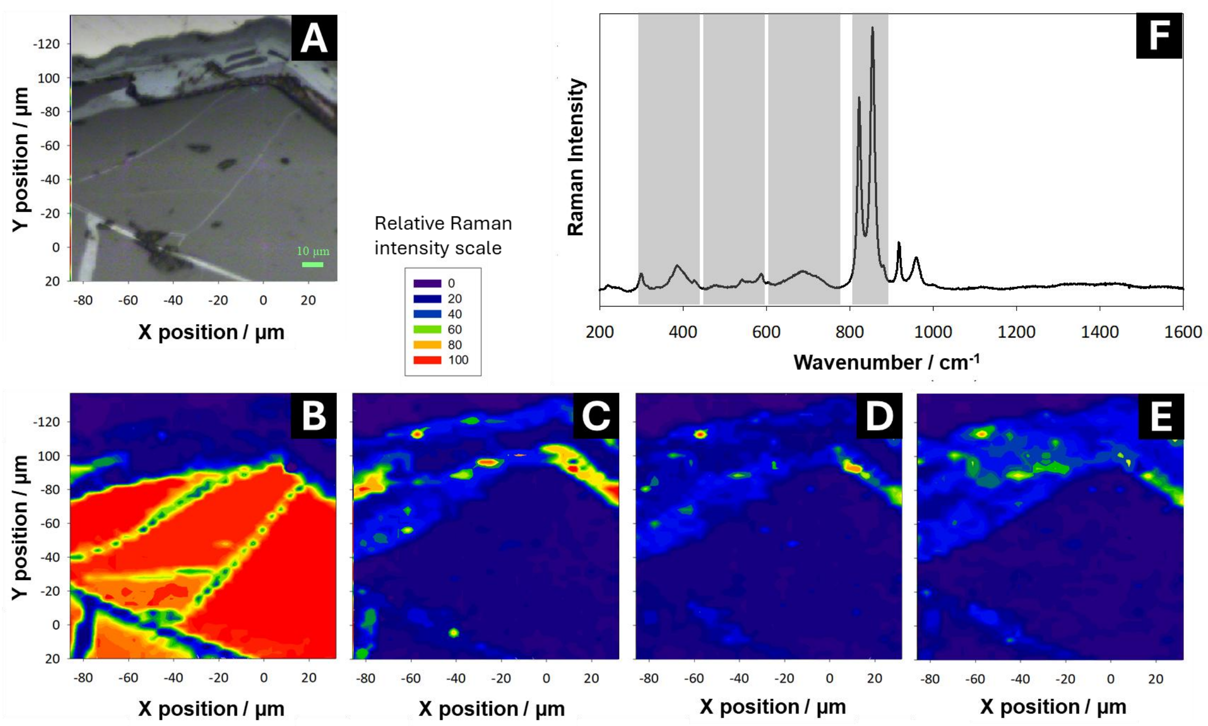

Figure 4. *(A) Micrography of the region of interest for Raman imaging at the interface between an olivine inclusion and the iron-nickel alloy, showing various microfractures and micrometric inclusions. (B-E) Raman images obtained by following the normalised intensity between 805 and 890* cm^{-1} *(B), 340-440* cm^{-1}*(C), 600-780* cm^{-1} *(D) and 450-600* cm^{-1}*(E). (F) Average spectrum obtained from the 1200 spectra of the Raman image showing in grey the range of wavenumbers for which the Raman images were generated.*

Generating these images requires a clear understanding of the expected mineralogy of the interrogated sample to define the wavenumber ranges of interest. Although the sample examined here is relatively simple (i.e., consisting of only four major constituents), producing these Raman images without that prior mineralogical knowledge would require the acquisition of a very significant number of individual spectra to form the Raman images. Alternatively, examination of the average spectrum would need to be performed wavenumber by wavenumber to identify regions of interest in imaging mode, an approach that is time-consuming. While this level of manual interpretation is feasible in a laboratory setting, it becomes impractical for rapid Raman imaging in the field, whether on Earth or during planetary surface mission operations. A more efficient data processing strategy is therefore necessary. In the following section, we explore the same dataset (1200 spectra recorded every 4 µm in the x and y directions on the region of interest shown in Figure 4A), using unsupervised principal component analysis (PCA) to facilitate data interpretation.

The data set was unwrapped, meaning that the 1200 spectra were treated as individual, unrelated spectra, and the spatial coordinates associated with each spectrum were not included as input for the PCA. To account for variations in relative intensity among mineral phases, all Raman spectra were normalised, and the PCA was performed relying on the correlation matrix. The analysis was performed within a few seconds on a standard office laptop and produced two key outputs: the loadings and the scores. The loadings describe the relationship between the original spectroscopic variables (wavenumbers) and the principal components (PCs), which are built as linear combinations of these original variables. The scores represent the projection of each spectrum onto the PCs, defining a new space where spectra are distributed according to their similarities and differences (spectra with similar values on the PCs will be closer to each other in terms of signal profiles). The first five PCs accounted for 73% of the total spectral variability in the dataset, with their respective scores and loadings (correlation) shown in Figure 5. The remaining PCs each contributed less than 2% of the total variance and were therefore disregarded in the subsequent discussion. The scores of the first five PCs allowed the identification of five distinct regions of interest, as illustrated in Figure 5. The scores indicate the contribution of each PC to the spectrum recorded at each pixel, with stronger coloration (assigned in the x-y coordinate of the associated spectrum in the initial Raman image) representing a higher contribution. The loadings help interpret how the spectroscopic variables influence the principal components. However, because the PCA was performed on the correlation matrix, all coefficients fall between -1 (strong anti-correlation) and 1 (strong correlation), making direct recognition of Raman spectral features less straightforward. To simplify the interpretation, pixels with similar scores (i.e. we used the PCA scores as a filter) were grouped, and their respective spectra were averaged, yielding five representative Raman spectra, as shown in Figure 5.

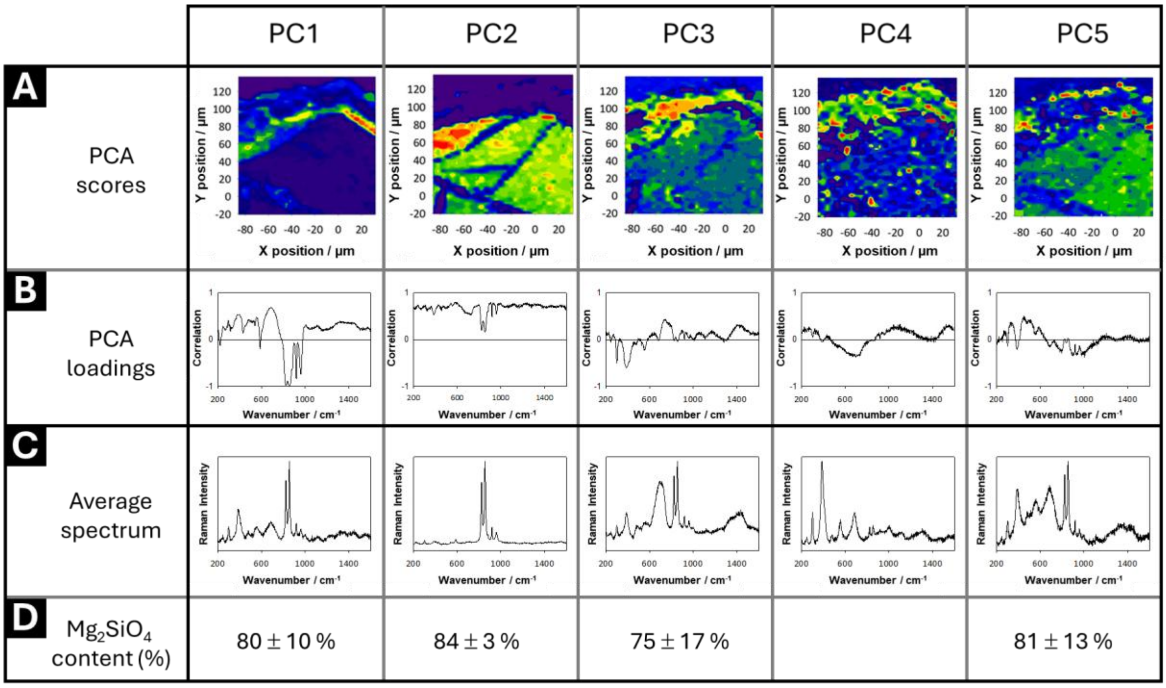

Figure 5. *Results of the Principal Component analysis (PCA) performed on the Raman image data set collected for the region of interest shown in Figure 4A. The columns correspond to the results associated to the first principal components (PC) accounting for more than 70% of the variability of the data set. (A) The score images obtained by reporting the scores associated with each PC at each coordinate (pixel) of the image. (B) The PCA loadings associated with each PC as calculated from the correlation matrix. (C) The average Raman spectra calculated from the Raman spectra associated with a score up to 0.7 (correlation) or lower than (anti-correlation) -0.7. (D) The forsterite (Mg_2SiO_4) molar fraction in the olivine for each region of interest defined by PC1, PC2, PC3 and PC5 applying the quantitative model based on the band position developed by Mouri at al. [19].*

The average Raman spectrum associated with PC2 (explaining 26% of the variance of the signal in the image) corresponds to olivine, and the PC2 image confirms that olivine is the main mineral in the inclusions. The PC2 image in Figure 5 closely resembles the Raman image in Figure 4B. Then, the average spectra associated with PC1 and PC5 (explaining 54 and 2% of the variance of the signal in the image respectively) are similar, both present the signatures of olivine and goethite, but with different intensity ratio. Interestingly, the PC1 image reveal that the goethite signal is especially higher along a fine layer at the olivine interface. The broad signal between 1200 and 1400 cm^{-1} observed with the 660 cm^{-1} broad band in the average spectrum associated to PC5 also indicates that disordered hematite can be associated with goethite and olivine. While the PC5 image suggests that iron oxyhydroxides are present inside the olivine inclusion. Their Raman signatures are anti-correlated with PC5, meaning that a decrease in the PC5 score corresponds to an increase in the spectral contribution of goethite and disordered hematite. This indicates that goethite and disordered hematite are primarily located in fractures within the olivine inclusion and in the outermost part of the inclusion at the interface with the alloy. Also, the average spectrum of PC4 (explaining 2% of the variance of the signal in the image) is dominated by the Raman signatures of goethite with minor contribution of disordered hematite (broad band at 660 cm^{-1}) and even less contribution of olivine. As shown in the PC4 image, the goethite is primarily located in the interface layer between the olivine core of the inclusion and the iron-nickel alloy. Finally, the average Raman spectrum associated with PC3 (explaining 4% of the variance of the signal in the image), corresponds to disordered hematite, with a contribution of olivine. The PC3 score image suggests that this mineral is concentrated in the central region of the iron oxyhydroxide layer. This region of interest aligns with the small dark-grey micrometric inclusions visible in the upper part of Figure 4A (context image).

Thus, the PCA analysis highlights that olivine (PC2) is the only statistically isolated mineral phase in the dataset. Goethite is either associated with olivine (PC1 and PC5) or disordered hematite (PC4), suggesting that iron oxyhydroxide formation is closely linked to olivine, which is separated from the Fe-Ni alloy by these minerals. Additionally, disordered hematite appears to be localised within micrometric olivine inclusions embedded in the iron oxyhydroxide layer between the inner olivine inclusion core and the Fe-Ni alloy.

Although PCA was used here to generate five Raman images, it is important to note that the analysis treated all spectra as randomly distributed. If the microstructure of the sample is not of interest to the operator, PCA can be applied only to reduce the dataset into a smaller subset of spectra while retaining the key spectral information. These results demonstrate that PCA effectively reduced the dataset from 1200 spectra to only five representative spectra, significantly minimizing the volume of data that would need to be transferred if PCA were applied by an astronaut during a planetary mission for instance.

Finally, using the Raman spectra filtered through PCA scores, we estimated the forsterite (Mg_2SiO_4) content of olivine in each region of interest where olivine was detected (i.e., associated with PC1, PC2, PC3, and PC5). The composition of olivine, which reflects the conditions under which it formed and the influence of minerals they are associated with, can be determined based on the position of the κ_1 band around 823 cm^{-1} [27]. By applying equation (1), where Fo is the forsterite (Mg_2SiO_4) molar fraction in the olivine, and κ_1 the position of the band, we obtained the values reported in Figure 5. These values are consistent with previously reported bulk analyses for the Sericho pallasite. However, our approach allows for spatially resolved characterisation of the olivine composition within the inclusion: the olivine is 5-10 % richer in magnesium at the centre of the inclusions than at the interface with the Fe-Ni alloy, where it is associated with iron oxyhydroxides. This observation has not been previously reported. As we observed here that the olivine associated with the iron oxyhydroxide formations in depleted in magnesium (i.e., richer in iron), it seems that the oxyhydroxide formations are originating to weathering of the iron-nickel alloy instead of the olivine inclusion.

$$Fo = -610.65 + 1.3981\,\kappa_1 - 0.00079869\,\kappa_1^2 \qquad (Eq.\ 1)$$

Conclusion

This study illustrates the efficiency of Principal Component Analysis (PCA) in processing Raman data for planetary exploration, condensing extensive datasets (here more than a thousand of spectra) into a subset of a few spectra, while retaining the essential mineralogical information. PCA is a practical tool for future robotic and human-led planetary exploration programs where data budgets are limited. Applied to the mineralogical characterisation of Sericho pallasite meteorite, PCA successfully identified olivine as the dominant phase and distinguished intricate iron oxyhydroxide formations at the olivine-metal interface. Integrating such data reduction methodologies into planetary mission training programs and payloads could facilitate more efficient *in-situ* analyses, improving sample selection for further interrogation using complementary techniques such as mass spectrometry. Moreover, in the context of Raman imaging, our results confirm that PCA enriches unsupervised Raman imaging interpretation. Using PCA scores as a filter allows rapid visualisation of mineral distributions and compositional variations, without necessitating extensive manual analysis. The polished section of Sericho pallasite constitutes an interesting training sample for future astronauts as part of the ESA's PANGAEA, even though current planetary missions are not aiming at interrogating flat polished sample surface.

Keywords

Raman spectroscopy, PCA, meteorite, olivine, planetary sciences.

Acknowledgements

C.M. and G.E. acknowledge financial support from the F.R.S.-FNRS (Fonds de la Recherche Scientifique - FNRS). I.B.H., HL. and M.M. acknowledge financial support from the UK Space Agency. The authors acknowledge the experimental work done by N. MILLIS recording the data.

Conflict of interest disclosure

The authors declare no conflict of interest.

References

[1] Wiens, R.C., Maurice, S., Robinson, S.H., et al. (2021) The SuperCam instrument suite on the NASA Mars 2020 rover: body unit and combined system tests. *Space Sci Rev.*, 217(1): 1-87. doi:10.1007/s11214-020-00777-5

[2] Beegle, L., Bhartia, R., White, M., DeFlores, L., Abbey, W., Wu, Y.H., Cameron, B., Moore, J.,

Fries, M., Burton, A., Edgett, K.S. (2015). SHERLOC: Scanning habitable environments with Raman & luminescence for organics & chemicals. *IEEE Aerospace Conference Proceedings*, 1–11. 10.1109/AERO.2015.7119105.

[3] Rull, F., Maurice, S., Hutchinson, I., Moral, A., Perez, C., Diaz, C., *et al.* (2017). The Raman laser spectrometer for the ExoMars rover mission to Mars. *Astrobiology*, *17*(6-7), 627-654. doi.org/10.1089/ast.2016.1567

[4] Michel, P., Ulamec, S., Böttger, U. *et al.* (2022). The MMX rover: performing in situ surface investigations on Phobos. *Earth Planets Space,* 74, 2. https://doi.org/10.1186/s40623-021-01464-7

[5] Wang, A., Jolliff, B. L., Lambert, J., & Hutchinson, I. (2024). Raman Spectroscopy for Lunar Sciences and Lunar Explorations. *LPI Contributions*, *3040*, 1274.

[6] Lerman, H. N., Hutchinson, I. B., McHugh, M., Wang, A., Jolliff, B. L., Parnell, J., & Armstrong, J. (2024). Testing of Analogue Planetary Materials with the Compact Integrated Raman Spectrometer. *LPI Contributions*, *3040*, 2592.

[7] Briones, C., Rodríguez-Manfredi, J. A., Kereszturi, A., & Mangold, N. (2025). Robotic Missions to Mars. In *Mars and the Earthlings: A Realistic View on Mars Exploration and Settlement* (pp. 51-84). Cham: Springer Nature Switzerland. https://doi.org/10.1007/978-3-031-66881-4_3

[8] Hutchinson, I. B., Ingley, R., Edwards, H. G., Harris, L., McHugh, M., Malherbe, C., & Parnell, J. (2014). Raman spectroscopy on Mars: identification of geological and bio-geological signatures in Martian analogues using miniaturized Raman spectrometers. *Philosophical Transactions of the Royal Society A: Mathematical, Physical and Engineering Sciences*, *372*(2030), 20140204. doi.org/10.1098/rsta.2014.0204

[9] Harris, L. V., McHugh, M., Hutchinson, I. B., Ingley, R., Malherbe, C., Parnell, J., ... & Edwards, H. G. (2015). Avoiding misidentification of bands in planetary Raman spectra. *Journal of Raman Spectroscopy*, *46*(10), 863-872. doi.org/10.1002/jrs.4667

[10] Rull, F., Veneranda, M., Manrique-Martinez, J. A., Sanz-Arranz, A., Saiz, J., Medina, J., ... & Lopez-Reyes, G. (2022). Spectroscopic study of terrestrial analogues to support rover missions to Mars–A Raman-centred review. *Analytica Chimica Acta*, *1209*, 339003. https://doi.org/10.1016/j.aca.2021.339003

[11] Demaret, L., Hutchinson, I. B., Ingley, R., Edwards, H. G., Fagel, N., Compere, P., ... & Malherbe, C. (2022). Fe-Rich Fossil Vents as Mars Analog Samples: Identification of Extinct Chimneys in Miocene Marine Sediments Using Raman Spectroscopy, X-Ray Diffraction, and Scanning Electron Microscopy–Energy Dispersive X-Ray Spectroscopy. *Astrobiology*, *22*(9), 1081-1098. 10.1089/ast.2021.0128

[12] Changela, H.G., Chatzitheodoridis, E., Antunes, A., *et al.* (2021). Mars: new insights and unresolved questions. *International Journal of Astrobiology*. 20(6), 394-426. doi:10.1017/S1473550421000276

[13] Stewart, S., Priore, R. J., Nelson, M. P., & Treado, P. J. (2012). Raman imaging. *Annual Review of Analytical Chemistry*, *5*(1), 337-360. https://doi.org/10.1146/annurev-anchem-062011-143152

[14] Guo, S., Popp, J., & Bocklitz, T. (2021). Chemometric analysis in Raman spectroscopy from experimental design to machine learning–based modeling. *Nature protocols*, *16*(12), 5426-5459. https://doi.org/10.1038/s41596-021-00620-3

[15] Sauro, F., Payler, S. J., Massironi, M., Pozzobon, R., Hiesinger, H., Mangold, N., ... & Bessone, L. (2023). Training astronauts for scientific exploration on planetary surfaces: The ESA PANGAEA programme. *Acta Astronautica*, *204*, 222-238. https://doi.org/10.1016/j.actaastro.2022.12.034

[16] Coccato, A., & Caggiani, M. C. (2024). An overview of Principal Components Analysis approaches in Raman studies of cultural heritage materials. *Journal of Raman Spectroscopy*, *55*(2), 125-147. doi.org/10.1002/jrs.6621

[17] Neo, Edward Ren Kai, et al. "A review on chemometric techniques with infrared, Raman and

laser-induced breakdown spectroscopy for sorting plastic waste in the recycling industry." *Resources, Conservation and Recycling* 180 (2022): 106217. https://doi.org/10.1016/j.resconrec.2022.106217

[18] J. Gattacceca, A. Bouvier, J. Grossman, K. Metzler, and M. Uehara, *Meteorit. Planet Sci*., 2019, 54, 469.

[19] Wallace, S., & Rafaelsen, J. (2018). Understanding the Possible Links Between Grain Boundary Morphology and Mineralogy in the Sericho Pallasite. *Microscopy and Microanalysis*, *24*(S1), 2114-2115. doi.org/10.1017/S1431927618011054

[20] J. S. Boesenberg, M. Humayun, R. Windmill, R. C. Greenwood, and I. Franchi, I. A., *LPI Contribution*, 2018, 2083.

[21] Hammer, Øyvind, and David AT Harper. "Past: paleontological statistics software package for educaton and data anlysis." *Palaeontologia electronica* 4.1 (2001): 1.

[22] Laetsch T, Downs R (2006) Software For Identification and Refinement of Cell Parameters From Powder Diffraction Data of Minerals Using the RRUFF Project and American Mineralogist Crystal Structure Databases. Abstracts from the 19th General Meeting of the International Mineralogical Association, Kobe, Japan, 23-28 July 2006. Available online at https://rruff.info/about/about_download.php (consulted September 2024).

[23] de Faria, D.L.A., Venâncio Silva, S. and de Oliveira, M.T. (1997), Raman microspectroscopy of some iron oxides and oxyhydroxides. *J. Raman Spectrosc.*, 28, 873-878. https://doi.org/10.1002/(SICI)1097-4555(199711)28:11<873::AID-JRS177>3.0.CO;2-B

[24] Marshall, C.P., Dufresne, W.J.B., Rufledt, C.J., (2020). Polarized Raman spectra of hematite and assignment of external modes. *Journal of Raman Spectroscopy*, 51(9), 1522-1529.

[25] Thibeau, R.J., Brown, C.W., and Heidersbach, R.H. (1978). Raman spectra of possible corrosion products of iron. *Appl. Spectrosc.* 32, 532–535.

[26] Hanesch, M. (2009) Raman spectroscopy of iron oxides and (oxy)hydroxides at low laser power and possible applications in environmental magnetic studies. *Geophys. J. Int.,* 177, 941–948. https://doi.org/10.1111/j.1365-246X.2009.04122.x

[27] Mouri, T., & Enami, M. (2008). Raman spectroscopic study of olivine-group minerals. *Journal of Mineralogical and Petrological Sciences*, *103*(2), 100-104.